Driving Force Control for In-Wheel Motor Electric Vehicles with Wheel Speed Limiter and Absolute Stability Analysis

Takumi Ueno, Binh-Minh Nguyen, Hiroshi Fujimoto
The University of Tokyo
5-1-5, Kashiwanoha, Kashiwa, Chiba, 277-8561, Japan
Email: ueno.takumi22@ae.k.u-tokyo.ac.jp

***Abstract*—To maintain the safe and accurate traction of electric vehicles (EVs), driving force control (DFC) has been studied for years. However, the traditional DFC requires the vehicle speed to calculate the reference of wheel speed. It increases the complexity and nonlinearity of the DFC system. Moreover, the saturation of the force controller's output challenges any attempt to design and analyze DFC systematically. To overcome these issues, this paper presents a novel DFC system in which the force controller directly outputs the wheel speed reference. It alleviates the system complexity, as the vehicle speed is only used to calculate the upper and lower bound of the wheel speed limiter. The proposed DFC configuration allows us to analyze system stability using the circle criterion to address the wheel speed saturation. The effectiveness of the proposed DFC and the stability analysis is verified by graphical tests, numerical simulations, and experiments using an in-wheel motor vehicle developed by our research group.**

***Index Terms*—absolute stability, electric vehicles, driving force control, in-wheel motor**

I. Introduction

As public eco-awareness increases, transportation shifts from traditional internal combustion engine vehicles (ICEVs) to electric vehicles (EVs). This shift has led to a lot of research, including wireless power transfer [1], energy storage [2], and energy management [3]. Moreover, due to the characteristics of the motor, EVs have some advantages regarding vehicle motion control, as shown below.

- The torque response is much faster than that of ICEVs.
- The motor torque can be measured from motor current.
- In-wheel motor vehicles control each wheel individually.

Thanks to the above merits, various advanced motion control methods have been studied for EVs. The typical are vibration suppression control [4], [5], lateral stability control [6], and range extension control [7]. This paper focuses on traction control, which guarantees the safe motion of the vehicle even if the road condition changes sharply.

From a literature review, there are many traction control systems for EVs, such as anti-skid control (ASC), slip ratio control (SRC), and driving force control (DFC). The ASC is a traction controller based on disturbance observer [8]. It has a simple structure and is easy to implement, but attaining reasonable control performance is too simple. By directly controlling the slip ratio, the SRC can overcome the demerit of the ASC [9], [10]. However, the limitation of the SRC is the capability to collaborate with other higher motion control layers because the reference value is the slip ratio. To overcome the limitation, the DFC has been developed since the last decade [11]–[13]. The DFC can suppress excessive tire slippage, generate driving force according to the reference value, and collaborate with other control layers.

Despite the great successes that have already been achieved, the following issues still need to be resolved for the development of DFC. The first is from an application point of view. In the original idea of the DFC, the control system is designed hierarchically, including the outer layer of force control and the inner layer of wheel speed control [11]. The force control layer outputs the slip ratio reference y^*. Then, the wheel speed reference ω^* is calculated from y^* with the vehicle speed. In addition, the driving force is not feedbacked directly but via a driving force observer (DFO). For this reason, the DFC system is quite complex and always nonlinear. This raises the second issue from a theoretical point of view. It is too complex to obtain a transfer function from y^* to the output of the DFO. In addition, there is a saturation of the signal y^*, which is placed between the two control layers. Consequently, designing and analyzing system performance and stability is still a challenge.

To overcome the issues above, the contribution of this paper is twofold. First, a novel DFC with a more straightforward configuration is proposed. In the proposed DFC, the force controller directly outputs the reference of the wheel speed ω^* to the inner layer. It simplifies the system configuration, as ω^* is not calculated from the vehicle speed V. Vehicle speed is only used to calculate upper and lower-bound wheel speeds. In other words, the vehicle speed does not participate in the dynamics of the inner layer. Second, this paper shows that obtaining a transfer function from ω^* to the estimated driving force is possible. Thanks to this model, the absolute stability analysis of the DFC system can be performed conveniently using circle criterion [14], [15]. The circle is to handle the wheel speed saturation, which is considered a time-varying nonlinear gain with sector-bound characteristics. With the criterion, the traditional force control of integral (I) can be easily extended to proportional-integral (PI) ones.

The remainder of this paper is organized as follows. In Section II, the modeling is formulated. In Section III, the proposed DFC is presented. In Section IV, the stability analysis

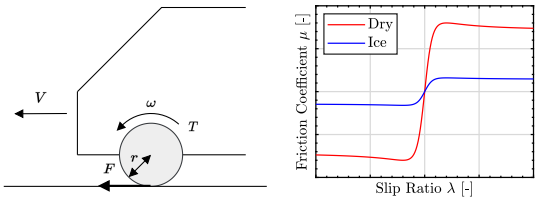

(a) Vehicle model. (b) μ–λ curve.

Fig. 1: Single-wheel vehicle model.

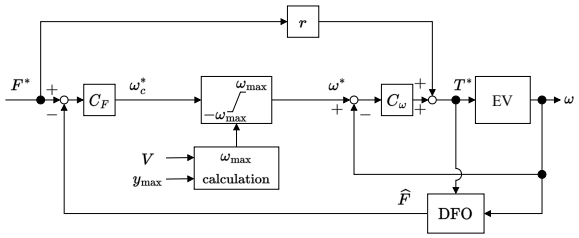

Fig. 2: Block diagram of the proposed DFC.

of the proposed DFC is shown. In Section V, the system design and analysis of DFC and the effectiveness of the proposed system are demonstrated by simulations and experiments. Finally, the conclusion is stated in Section VI.

II. Vehicle Model

This paper focuses on the single-wheel vehicle model to develop an idea for the new DFC. Fig. 1(a) shows the longitudinal vehicle model and tire rotational dynamics. The equations of each motion are expressed as

$$M\dot{V} = F \tag{1}$$

$$J\dot{\omega} = T - rF \tag{2}$$

where M, V, F, J, ω, r, and T are vehicle mass, vehicle velocity, driving force, wheel moment of inertia, wheel speed, wheel radius, and motor torque, respectively. As an indicator of the degree of tires' slippage, the slip ratio is defined as

$$\lambda = \frac{V_\omega - V}{\max(V_\omega, V, \epsilon)} \tag{3}$$

where V_ω is calculated as $V_\omega = r\omega$ and ϵ is a small positive value preventing the zero division. Fig. 1(b) shows the relationship between the driving force and the slip ratio called Paceijka's magic formula [16]. It has nonlinear characteristics, and the relationship also occurs in some complexity of vehicle motion control. Since the definition of λ for acceleration differs from that for deceleration, λ is inconvenient to control. Thus, in the traditional DFC approach [11], the control input y, defined as follows, is controlled instead of the slip ratio.

$$y = \frac{V_\omega}{V} - 1. \tag{4}$$

It is the same definition as the slip ratio for deceleration. The relationship between λ and y in the domain of $\lambda > 0$ is calculated as

$$y = \frac{\lambda}{1-\lambda} \tag{5}$$

which indicates that y almost equals to λ when λ is small.

III. Proposed DFC

This section shows the idea of directly controlling the wheel speed and the control system. Fig. 2 shows the block diagram of the proposed DFC. The DFC has a cascade structure with a force controller C_F in the outer layer and a wheel speed controller C_ω in the inner layer.

A. Idea of direct wheel speed control

In general DFC system, the driving forces are fed back through the driving force observer (DFO), which utilizes the motor torque and the angular velocity of the wheels as

$$\hat{F}(s) = Q_F(s)\frac{T(s) - Js\omega(s)}{r} \tag{6}$$

where $Q_F(s) = 1/(\tau s + 1)$ is the low pass filter of the DFO. From (2), if the driving force reference is given as $T^* = rF^*$ and the estimated driving force is given by (6), the reference wheel speed can be calculated as

$$\omega^* = \int \frac{r}{J}(F^* - \hat{F})dt. \tag{7}$$

which can be seen as an integral control. Thus, it is reasonable to generate the wheel speed reference from C_F directly.

B. Control system

In the traditional DFC, the wheel speed reference of C_ω is calculated from y^* with the vehicle speed measurement V, which always makes the system nonlinear. On the other hand, in the proposed DFC, the vehicle velocity is only used to calculate the upper-bound of the wheel speed limiter by replacing the output of the C_ω with wheel speed, which is given as

$$\omega_{\max} = (1 + y_{\max})\frac{V}{r} \tag{8}$$

where $y_{\max}$ shows the limiter of y.

In addition, the wheel speed controller is the same as the traditional controller as

$$C_\omega(s) = K_{\omega P} + \frac{K_{\omega I}}{s} \tag{9}$$

where $K_{\omega P}$ and $K_{\omega I}$ are proportional and integral gains of the wheel speed controller, respectively. As seen from Fig. 2 and [11], the control performance of the proposed DFC is the same as the traditional DFC, but the following criterion can be easily applied to the proposed DFC. Further, the force controller can be extended from the integral controller in the traditional DFC to other types of controllers, such as the proportional-integral ones, as

$$C_F(s) = K_{FP} + \frac{K_{FI}}{s} \tag{10}$$

where K_{FP} and K_{FI} are the proportional and integral gains of the force controller.

IV. Stability analysis

This section will obtain a transfer function of the inner loop from the after ω^* to before ω_c^* wheel speed limiter, and the analysis of the proposed DFC is designed with the Nyquist plot.

A. Derivation of the transfer function for stability analysis

First, we will obtain a transfer function of the inner loop from the speed reference ω^* to the estimated driving force $\hat{F}$. Solving the slip ratio definition equation (3) for ω and differentiating it, the angular acceleration during driving and braking is calculated as

$$\dot{\omega} = \begin{cases} \dfrac{\dot{V}}{r}\dfrac{1}{1-\lambda} + \dfrac{\dot{\lambda}V}{r}\dfrac{1}{(1-\lambda)^2} \\ \dfrac{\dot{V}}{r}(1+\lambda) + \dfrac{\dot{\lambda}V}{r}. \end{cases} \tag{11}$$

In addition, substituting (1) and (2) into (11), the motor torque can be expressed as

$$T = \begin{cases} \left(r + \dfrac{J}{Mr}\dfrac{1}{1-\lambda}\right)F + \dfrac{J\dot{\lambda}V}{r}\dfrac{1}{(1-\lambda)^2} \\ \left(r + \dfrac{J}{Mr}(1+\lambda)\right)F + \dfrac{J\dot{\lambda}V}{r}. \end{cases} \tag{12}$$

Here, if the slip ratio has a small value, the relationship between λ and y can be approximately expressed as

$$\frac{1}{1-\lambda} \approx 1 + \lambda \approx 1 + y. \tag{13}$$

Substituting (13) into (12) and normalizing it with the nominal parameters and nominal slip ratio y_n, the following relationship is obtained as

$$T = \left(r_n + \frac{J_n}{M_n r_n}(1+y_n)\right)F \tag{14}$$

where the subscript n indicates the nominal parameter. Considering the wheel speed control loop and (2), the motor torque is given as

$$\begin{aligned} &T(s) = C_\omega(s)\{\omega^*(s) - P_\omega(s)(T(s) - rF(s))\} \\ \Rightarrow\ &T(s) = \frac{C_\omega(s)}{1 + C_\omega(s)P_\omega(s)}\omega^*(s) + \frac{r_n C_\omega(s)P_\omega(s)}{1 + C_\omega(s)P_\omega(s)}F(s) \end{aligned} \tag{15}$$

where $P_\omega = 1/Js$. Substituting (2), (6), and (14) into (15), the transfer function from the reference wheel speed ω^* to the estimated driving force $\hat{F}$ is derived as

$$\begin{aligned} G(s) &= \frac{\hat{F}(s)}{\omega^*(s)} \\ &= \frac{Q_F(s)C_\omega(s)}{\{r_n + \frac{J_n}{M_n r_n}(1+y_n)\} + \frac{J_n}{M_n r_n}(1+y_n)C_\omega(s)P_\omega(s)}. \end{aligned} \tag{16}$$

Here, we can analyze the system stability assuming a nominal y_n. Thanks to (16), the stability of the DFC system can be analyzed via the feedback connection of $H(s) = G(s)C_F(s)$ and the speed saturation (Fig. 3). Substituting $Q_F(s)$, $P_\omega(s)$, (10), and (9) to $H(s)$, it can be rewriten as

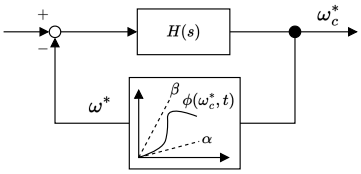

Fig. 3: Equivalent block diagram of DFC.

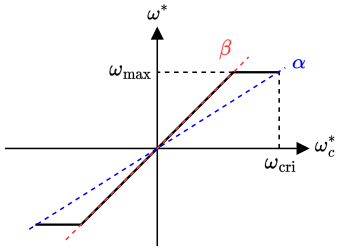

Fig. 4: Wheel speed limiter with sector-bound.

$$H(s) = \frac{1}{\tau s + 1}\frac{J_n(K_{\omega P}s + K_{\omega I})(K_{FP}s + K_{FI})}{(r_n + \xi)J_n s^2 + \xi(K_{\omega P}s + K_{\omega I})} \tag{17}$$

where $\xi = J_n(1 + y_n)/M_n r_n$. Applying Routh–Hurwitz stability criterion, $H(s)$ is shown to be Hurwitz if the stable poles are assigned to the speed control loop and the force controllers are designed with positive gains.

B. Application of circle criterion to DFC

The absolute stability of the proposed DFC can be discussed via the equivalent system in Fig. 3. As presented in [14], the saturation block with the input ω_c^* and the output ω^* can be treated as a time-varying nonlinear gain ϕ which belongs to a specific sector bound $[\alpha, \beta]$. For example,

$$\alpha \le \phi(\omega_c^*, t) \le \beta. \tag{18}$$

As shown in Fig. 4, the wheel speed limiter belongs to the sector with the upper-bound $\beta = 1$. The lower-bound α can be selected from 0 to 1. Needless to say, $\alpha = 1$ is the trivial case as it makes the limiter disappear. As described in the previous subsection, $H(s)$ is Hurwitz. Therefore, the following two design conditions can be considered.

- Condition 1 ($\alpha = 0$): The DFC system is absolutely stable if the $H(j\omega)$ Nyquist plot lies to the right of the vertical line defined by $Re[s] = -1$.
- Condition 2 ($0 < \alpha < 1$): The DFC system is absolutely stable if the Nyquist plot of $H(j\omega)$ does not enter the disk $D(\alpha, \beta)$ defined in Fig. 5.

V. Evaluation and discussion

In this section, the DFC system is designed based on the theoretical conditions obtained in the previous section. The proposed system is evaluated by simulations and experiments

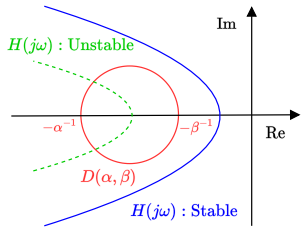

Fig. 5: Circle criterion ($0 < \alpha < \beta$). The red line shows the circle $D(\alpha, \beta)$, and the blue and green lines show the $H(s)$ Nyquist plots for stable and unstable cases, respectively.

using an in-wheel motor electric vehicle developed by our research group (Fig. 6). The main parameters of the vehicle and in-wheel motors are summarized in Table I.

A. System design and analysis

In this paper, we only focus on the design of the force controller. The wheel speed control is designed by pole placement to the close loop system, including the nominal transfer function $P_\omega(s) = 1/Js$ and the PI controller $C_\omega(s)$. Through a fine-tuning process, the proportional and integral gains of the wheel angular velocity controller C_ω are selected as 50.476 and 504.76, respectively. On the other hand, the time constant of the low pass filter is selected as $\tau = 0.03$.

Firstly, we examine Condition 1, which requires the selection of $\alpha = 0$. For the sake of simplicity, we consider the force controller of the integral type. As shown in Fig. 7(a), the maximum K_{FI} that satisfies Condition 1 is 0.0023. However, this integral gain value cannot guarantee good driving force control performance. As described in Fig. 7(b), the estimated driving force cannot follow the reference value with $K_{FI} = 0.0023$.

Due to the above reason, we should utilize Condition 2. In other words, the best we can hope for is to show absolute stability with a finite domain. To this end, we will select a reasonable value of the lower-bound α. In Fig. 4, $\omega_{\max}$ is

TABLE I: Vehicle and in-wheel motor specifications.

Symbol	Description	Value
M	Vehicle mass	925 kg
r	Wheel radius	0.302 m
J	Inertia of rear wheel	1.26 kgm^2
–	Rated and maximum torque	137 Nm, 340 Nm
–	Rated and maximum power	4.30 kW, 10.7 kW
–	Rated and maximum speed	300 rpm, 1500 rpm

Fig. 6: FPEV-2 Kanon.

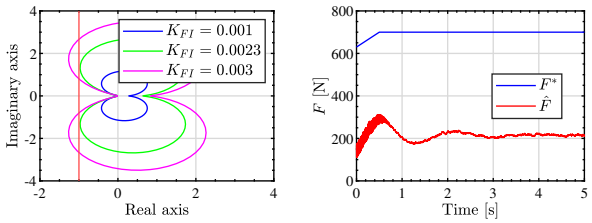

(a) (b)

Fig. 7: (a) Stability analysis using Condition 1, (b) Simulation result of driving force ($K_{FI} = 0.0023$).

calculated by (8). Since the slip limiter $y_{\max}$ is usually small, we can let $\lambda_s = y_{\max}$ and approximate as

$$\omega_{\max} = \frac{1}{(1-\lambda_s)}\frac{V}{r}. \tag{19}$$

With the integral force control, the command ω_c^* can be expressed as

$$\begin{aligned} \omega_c^* &= \frac{K_{FI}}{s}(F^* - \hat{F}) = \frac{K_{FI}}{r}\frac{1}{s}(rF^* - r\hat{F}) \\ \Rightarrow \frac{r}{K_{FI}}\dot{\omega}_c^* &= rF^* - r\hat{F}. \end{aligned} \tag{20}$$

Let $\tilde{J} = r/K_{FI}$ and $T^* = rF^*$, we have

$$\tilde{J}\dot{\omega}_c^* = T^* - r\hat{F}. \tag{21}$$

The above equation resembles the wheel's rotational dynamics (2). It means the force controller operates as a "virtual wheel." Thus, the critical speed ω_{cri} in Fig. 4 can be calculated with a critical slip ratio λ_{cri} of the "virtual wheel." This critical speed can be assumed as

$$\omega_{\text{cri}} = \frac{1}{(1-\lambda_{\text{cri}})}\frac{V}{r}. \tag{22}$$

Consequently, the value of α can be calculated as

$$\alpha = \frac{\omega_{\max}}{\omega_{\text{cri}}} = \frac{1-\lambda_{\text{cri}}}{1-\lambda_s}. \tag{23}$$

Although not specified in this paper in Fig. 2, safety measures such as setting the torque to zero and stopping the experiment when $\lambda = 0.7$ is exceeded are also necessary for experiments. It is reasonable to select $\lambda_s = 0.05$ and $\lambda_{\text{cri}} = 0.7$. Thus, lower-bound α can be approximately selected as 0.3. Concerning the sector $[0.3, 1]$, in the following, we will evaluate three candidates for the force controllers.

- Case A: $K_{FI} = 0.2$ (a relatively small integral gain)
- Case B: $K_{FI} = 2.0$ (a relatively big integral gain)
- Case C: $K_{FI} = 2.0$ and $K_{FP} = 0.02$ (PI controller)

Based on the circle criterion, graphical tests of three cases are shown in Fig. 8. The system is stable in Case A as $H(j\omega)$ does not enter disk D. However, as shown in the green line, the system becomes unstable when the gain becomes more significant (Case B). Fortunately, introducing a small proportional gain can recover the system's stability. It is the graphical test result of Case C, as shown by the pink line.

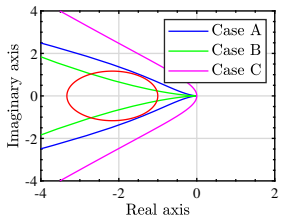

Fig. 8: Stability analysis using Condition 2.

B. Simulation result

Figs. 9 and 10 show the simulation results of the driving force and wheel speed for three cases, respectively. The estimated driving force in the integral controller with small feedback gain (Case A) shows no oscillation or divergence. It is consistent with the stability analysis results using the circle criterion shown in Fig. 8. However, the control performance is relatively poor as the driving force does not match the reference value. Thus, we increase the integral gain to attain better control performance. Unfortunately, the system becomes unstable if the integral gain is quite significant (Case B). As shown in Fig. 8, the Nyquist plot enters the disk. Consequently, the DFC system suffers severe vibration as shown in Figs. 9(b) and 10(b). The problem can be solved by introducing a small proportional gain (Case C). Fig. 8 shows that the Nyquist plot does not enter the disk, and the system has enough stability margin. Consequently, the driving force and wheel speed can follow the reference value without fluctuation, as demonstrated in Figs. 9(c) and 10(c). The simulation results also show that the circle criterion can be used to predict control performance.

C. Experimental result

Figs. 11 and 12 show the experimental results of the driving force and wheel speed for three test cases, respectively. As in the simulation results, when the integral gain is small (Case A), the estimated driving force does not follow the reference value sufficiently. When the integral gain increases (Case B), the system produces a vibration phenomenon. Due to the introduction of the proportional gain (Case C), the system stability is recovered, and the control performance of Case C is much better in comparison with Cases A and B.

VI. Conclusion

This paper proposes a novel DFC in which the force controller directly generates the wheel speed reference. The proposed DFC simplifies the system configuration, as it is unnecessary to calculate the wheel speed reference using the vehicle speed. Furthermore, using the circle criterion, the proposed DFC allows us to formulate the system's transfer function for stability analysis. Due to the circle stability condition, we have a convenient graphical test for designing and tuning the controller. Simulation and experiment results are consistent with the proposed stability condition. In the future, we will apply the proposed method to range extension control and direct yaw moment control.

Acknowledgment

This research was partly supported by Industrial Technology Research Grant Program from New Energy and Industrial Technology Development Organization (NEDO) of Japan (number 05A48701d), the Ministry of Education, Culture, Sports, Science and Technology grant (number 22246057 and 26249061).

References

[1] K. V. Chowdary, K. Kumar, R. K. Behera, and S. Banerjee, "Overview and analysis of various coil structures for dynamic wireless charging of electric vehicles," in *2020 IEEE international conference on power electronics, smart grid and renewable energy (PESGRE2020)*. IEEE, 2020, pp. 1–6.

[2] V. Mali, R. Saxena, K. Kumar, A. Kalam, and B. Tripathi, "Review on battery thermal management systems for energy-efficient electric vehicles," *Renewable and Sustainable Energy Reviews*, vol. 151, p. 111611, 2021.

[3] B-M. Nguyen, J. P. F. Trovão, and M. C. Ta, "Double-layer energy management for multi-motor electric vehicles," *IEEE Transactions on Vehicular Technology*, 2023.

[4] T. Suzuki, M. Mae, T. Takeuchi, H. Fujimoto, and E. Katsuyama, "Model-based filter design for triple skyhook control of in-wheel motor vehicles for ride comfort," *IEEJ Journal of Industry Applications*, vol. 10, no. 3, pp. 310–316, 2021.

[5] H. Fuse, H. Fujimoto, K. Sawase, N. Takahashi, R. Takahashi, Y. Okamura, and R. Koga, "Derivation of dynamic model of two-input-two-output torque difference amplification motor drive system and independent left-and-right wheel control with decoupling compensator," *IEEJ Journal of Industry Applications*, vol. 11, no. 3, pp. 427–436, 2022.

[6] K. Nam, H. Fujimoto, and Y. Hori, "Design of an adaptive sliding mode controller for robust yaw stabilisation of in–wheel–motor–driven electric vehicles," *International Journal of Vehicle Design*, vol. 67, no. 1, pp. 98–113, 2015.

[7] Y. Zhang, Y. Zhang, Z. Ai, Y. L. Murphey, and J. Zhang, "Energy optimal control of motor drive system for extending ranges of electric vehicles," *IEEE Transactions on Industrial Electronics*, vol. 68, no. 2, pp. 1728–1738, 2021.

[8] H. Fujimoto, T. Saito, A. Tsumasaka, and T. Noguchi, "Motion control and road condition estimation of electric vehicles with two in-wheel motors," in *Proceedings of the 2004 IEEE International Conference on Control Applications, 2004.*, vol. 2. IEEE, 2004, pp. 1266–1271.

[9] Y. Ma, J. Zhao, H. Zhao, C. Lu, and H. Chen, "Mpc-based slip ratio control for electric vehicle considering road roughness," *IEEE Access*, vol. 7, pp. 52 405–52 413, 2019.

[10] D. Savitski, V. Ivanov, K. Augsburg, T. Emmei, H. Fuse, H. Fujimoto, and L. M. Fridman, "Wheel slip control for the electric vehicle with in-wheel motors: Variable structure and sliding mode methods," *IEEE Transactions on Industrial Electronics*, vol. 67, no. 10, pp. 8535–8544, 2019.

[11] M. Yoshimura and H. Fujimoto, "Driving torque control method for electric vehicle with in-wheel motors," *Electrical Engineering in Japan*, vol. 181, no. 3, pp. 49–58, 2012.

[12] T. Ueno, B-M. Nguyen, and H. Fujimoto, "Direct yaw moment control for electric vehicles with variable-rate-slip-ratio-limiter based driving force control," in *2023 IEEE International Conference on Mechatronics (ICM)*. IEEE, 2023, pp. 1–6.

[13] T. Ueno, H. Pousseur, B-M. Nguyen, A. C. Victorino, and H. Fujimoto, "Proposal of on-board camera-based driving force control method for autonomous electric vehicles," in *2023 IEEE/ASME International Conference on Advanced Intelligent Mechatronics (AIM)*. IEEE, 2023, pp. 424–429.

[14] H. K. Khalil, *Nonlinear systems*. Prentice-Hall, 2002.

[15] B-M. Nguyen, T. Kobayashi, K. Sekitani, M. Kawanishi, and T. Narikiyo, "Altitude control of quadcopters with absolute stability analysis," *IEEJ Journal of Industry Applications*, vol. 11, no. 4, pp. 562–572, 2022.

[16] H. B. Pacejka and E. Bakker, "The magic formula tyre model," *Vehicle system dynamics*, vol. 21, no. S1, pp. 1–18, 1992.

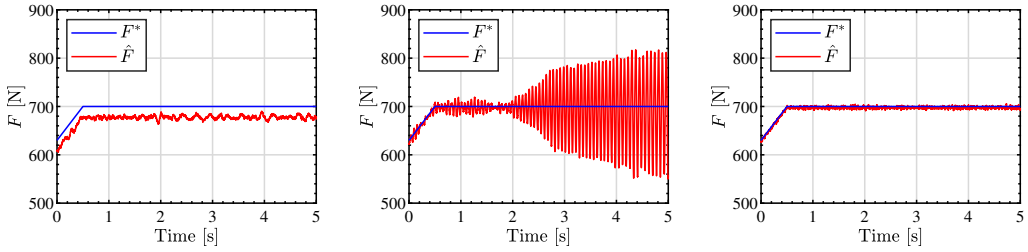

(a) Case A. (b) Case B. (c) Case C.

Fig. 9: Simulation result of the driving force.

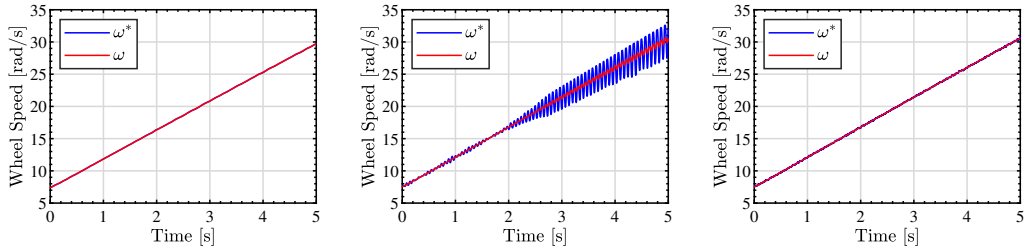

(a) Case A. (b) Case B. (c) Case C.

Fig. 10: Simulation result of the wheel speed.

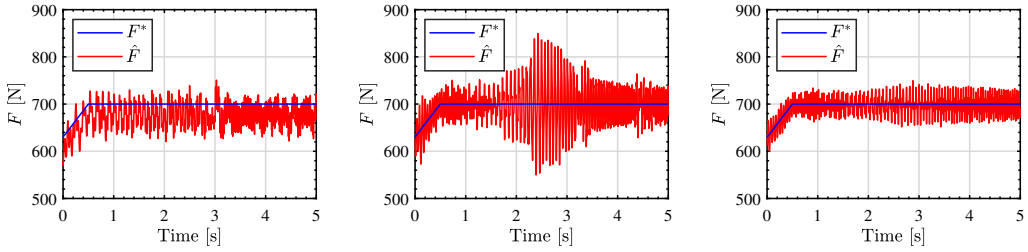

(a) Case A. (b) Case B. (c) Case C.

Fig. 11: Experimental result of the driving force.

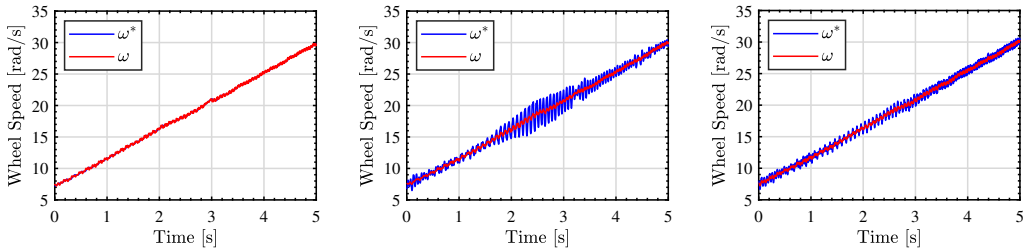

(a) Case A. (b) Case B. (c) Case C.

Fig. 12: Experimental result of the wheel speed.